

# Scaled Block Vecchia Approximation for High-Dimensional Gaussian Process Emulation on GPUs

Qilong Pan<sup>1,5</sup>, Sameh Abdulah<sup>1,5</sup>, Mustafa Abduljabbar<sup>1,5</sup>, Hatem Ltaief<sup>1,5</sup>, Andreas Herten<sup>2,6</sup>,  
Mathis Bode<sup>2,7</sup>, Matthew Pratola<sup>3,8</sup>, Arindam Fadikar<sup>4,9</sup>, Marc G. Genton<sup>1,5</sup>,  
David E. Keyes<sup>1,5</sup>, Ying Sun<sup>1,5</sup>

<sup>1</sup>King Abdullah University of Science and Technology, Thuwal, KSA

<sup>2</sup>Jülich Supercomputing Centre (JSC), Jülich, Germany

<sup>3</sup>Indiana University, Bloomington, IN, USA

<sup>4</sup>Argonne National Laboratory, Lemont, IL, USA

<sup>5</sup>{Firstname.Lastname}@kaust.edu.sa <sup>6</sup>a.herten@fz-juelich.de

<sup>7</sup>m.bode@fz-juelich.de <sup>8</sup>mpratola@iu.edu <sup>9</sup>afadikar@anl.gov

## Abstract

Emulating computationally intensive scientific simulations is essential to enable uncertainty quantification, optimization, and decision-making at scale. Gaussian Processes (GPs) offer a flexible and data-efficient foundation for statistical emulation, but their poor scalability limits applicability to large datasets. We introduce the Scaled Block Vecchia (SBV) algorithm for distributed GPU-based systems. SBV integrates the Scaled Vecchia approach for anisotropic input scaling with the Block Vecchia (BV) method to reduce computational and memory complexity while leveraging GPU acceleration techniques for efficient linear algebra operations. To the best of our knowledge, this is the first distributed implementation of any Vecchia-based GP variant. Our implementation employs MPI for inter-node parallelism and the MAGMA library for GPU-accelerated batched matrix computations. We demonstrate the scalability and efficiency of the proposed algorithm through experiments on synthetic and real-world workloads, including a 50M point simulation from a respiratory disease model. SBV achieves near-linear scalability on up to 64 A100 and GH200 GPUs, handles 320M points, and reduces energy use relative to exact GP solvers, establishing SBV as a scalable and energy-efficient framework for emulating large-scale scientific models on GPU-based distributed systems.

## Keywords

Batched Linear Algebra, Energy-Efficient HPC, Gaussian Processes, GPU Computing, High-Dimensional Data, Scalable Emulation, Vecchia Approximation

## 1 Introduction

Many modern scientific and engineering advances rely on the use of computer models that use mathematical equations to represent physical systems and are implemented as high-fidelity simulations. These models allow researchers to explore phenomena that are impractical to observe experimentally, such as climate dynamics [13, 25], materials [9, 41], and cosmological structure formation [26, 37, 38]. Computer models can generate predictions that guide policy decisions, technological innovation, and fundamental discovery by solving systems of differential equations or leveraging particle-based methods [9, 13, 37]. However, when exploring models with many input parameters, learning the relationship between inputs and outputs may require thousands of evaluations [17]. Such high

computational costs often constrain their usage, motivating the adoption of statistical emulators to approximate the simulator’s behavior at a fraction of the cost [2, 35].

A common approach to building computer model emulators involves fitting a Gaussian Process (GP) to data generated by running the simulator at a predefined set of input values (design points), effectively learning a mapping from the model input space to the model output space [7]. GP-based emulators improve interpretability and enable efficient analysis, especially when simulating scenarios across a wide parameter space. For example, variable importance [27, 33] and sequential optimization [42] may only be feasible using a cheap-to-evaluate GP emulator of the underlying expensive-to-evaluate simulator.

However, GPs face significant scalability challenges due to their  $O(n^3)$  computational cost and  $O(n^2)$  memory requirements, where  $n$  is the number of data points. These costs arise from operations on a dense  $n \times n$  covariance matrix that captures the correlations between data inputs. [4]. For instance, modeling 200K locations demands about 300 GB of memory and an estimated 2.6 PFLOP of computation, making standard GPs infeasible for large-scale applications without approximation methods. Thus, numerous studies have addressed the computational and memory challenges of large-scale GPs. Some efforts have pursued exact GP computation on High Performance Computing (HPC) systems [3, 4, 6]. For instance, the largest reported problem size was processed on ORNL’s Frontier system, handling 27.24M data points in mixed-precision across approximately 9K nodes (~36K AMD GPUs) of the system [2]. However, most of the literature has focused on approximation to alleviate the computational burden of GP modeling, including low-rank [8, 18, 36], tile low-rank [5, 28, 34], covariance tapering [18], and Vecchia approximations [22, 30].

Among these approximation methods, Classic Vecchia (CV) approximation demonstrates superior advantages [21]. In [24], Katzfuss et al. introduced the Vecchia approximation for GP emulation in the context of computer experiments and proposed the Scaled Vecchia (SV) method to enhance approximation accuracy in high-dimensional settings. However, their study was limited to small-scale problems and relied entirely on CPU-based computations. In contrast, efforts have been made to accelerate the classic Vecchia algorithm on GPUs, such as in [30], which subsequently introduced the Block Vecchia (BV) approach [31] to enhance computational speed further while preserving approximation accuracy.

Nevertheless, the use of CV approximation for high-dimensional GP emulation on GPUs remains unexplored. This gap presents an opportunity to develop a scalable GPU-based method capable of efficiently addressing the computational and memory challenges posed by high-dimensional inputs.

In this work, we propose a novel algorithm called the Scaled Block Vecchia (SBV) approximation for distributed GPU-based systems. SBV integrates the Block Vecchia (BV) algorithm from [31] with the Scaled Vecchia approach introduced in [24], while leveraging GPU acceleration techniques from [30]. To the best of our knowledge, this work represents the first distributed implementation of any variant of the Vecchia-based GP algorithm. Leveraging the Message Passing Interface (MPI), we parallelize computations across multiple GPU-enabled nodes, enabling scalable performance well beyond the capabilities demonstrated in prior studies.

To validate the accuracy and robustness of our algorithm, we perform GP simulations across a range of parameter settings and benchmark its performance on the satellite drag dataset, a standard high-dimensional testbed for evaluating GP-based models [39]. As an application in computer model emulation, we apply our algorithm to MetaRVM, a compartmental simulation model designed for generic respiratory virus diseases [15]. Experimental results demonstrate both high predictive accuracy and strong scalability, with successful runs on up to 64 A100/GH200 GPUs and problem sizes reaching 320M data points. Additionally, our approach achieves a noticeable reduction in power consumption compared to the state-of-the-art exact GP framework on GPUs, i.e., ExaGeoStat [4].

The paper is organized as follows: Section 2 summarizes the main contributions of the study. Section 3 provides a brief overview of related work. Section 4 presents the necessary background. Section 5 details the proposed algorithm. Section 6 describes the simulation study and reports the results of the computer model application. Section 7 focuses on performance evaluation and analysis. Finally, conclusions are presented in Section 8.

## 2 Contributions

The key contributions of this work are as follows:

- We propose the Scaled Block Vecchia (SBV) approximation, a novel GP algorithm that integrates anisotropic input scaling with block-based conditioning to reduce both computational and memory complexity. SBV improves approximation accuracy in high-dimensional GPs.
- We develop the first distributed implementation of any Vecchia-based GP variant designed for modern GPU-accelerated HPC systems. Our implementation employs MPI for inter-node parallelism and the MAGMA library for fine-grained batched GPU-accelerated linear algebra operations.
- We benchmark SBV on synthetic datasets and the high-dimensional satellite drag dataset, demonstrating substantial improvements in runtime and predictive accuracy over state-of-the-art GP approximation methods.
- We use and assess SBV to emulate the MetaRVM epidemiological simulation using 50M samples and 10-dimensional inputs, achieving high predictive accuracy and practical scalability.

- We demonstrate both weak and strong scaling on the JURECA-DC GPU (AMD EPYC + A100) and JEDI (GH200 Superchip) systems at Jülich Supercomputing Centre (JSC), with experiments scaling up to 64 nodes and problem sizes reaching up to 320M data points.
- We perform a comprehensive energy analysis across GPU platforms, showing that SBV significantly reduces power consumption compared to exact GP frameworks such as ExaGeoStat while maintaining high throughput and accuracy.

## 3 Related Work

**GP emulators:** GPs are widely used for emulating high-fidelity simulators in scientific computing, with applications in cosmology [38], climate modeling [2], and mechanism science [39]. Notable examples include emulation of N-body cosmological simulations [26], particle-material interactions [41], and epidemiological models of disease spread [14]. While recent advances in scalable GPs have improved performance, few approaches offer distributed, multi-GPU implementations. The proposed SBV algorithm directly addresses this gap by enabling efficient, scalable GP emulation on distributed, GPU-accelerated HPC systems.

**CV approximation:** CV approximation [22, 23, 40] reduces the computational complexity of GPs by factorizing the joint distribution into a product of conditional distributions. Recent advancements have enhanced the effectiveness of the CV approximation through improved data point ordering and neighbor selection [20]. The BV approximation [31] builds on this by conditioning on blocks of observations rather than individual points, enabling batched linear algebra operations on GPUs and improving throughput and memory efficiency in high-performance environments [30]. More recently, the SV method was introduced to address challenges associated with high-dimensional inputs by applying anisotropic input scaling [24], which enables the model to capture directional-varying correlations. Our work extends these developments by integrating block-based conditioning and anisotropic scaling into a unified framework, i.e., SBV, and presenting a distributed implementation optimized for multi-GPU systems.

## 4 Background

This section provides background on GPs, the BV approximation, Kullback–Leibler (KL) divergence, and the scaled kernel function, which together form the foundation for our proposed extension for high-dimensional data. Table 1 summarizes the abbreviations used throughout the paper to enhance clarity and readability.

**Table 1: List of abbreviations and their explanations.**

Abbreviation	Explanation
GPs	Gaussian Processes
CV/SV/BV/SBV	Classic/Scaled/Block/Scaled Block Vecchia
$n/n^*$	Problem size in estimation/prediction
$bs_{est}/bc_{est}$ ( $bs/bc$ )	Block (batched) size/count for estimation
$bs_{pred}/bc_{pred}$ ( $bs^*/bc^*$ )	Block (batched) size/count for prediction
$m_{est}/m_{pred}$	# nearest neighbors for estimation/prediction

#### 4.1 Gaussian Processes (GPs)

GPs provide a flexible framework for modeling and predicting functions across low- and high-dimensional input spaces. Let  $\mathbf{X} = [\mathbf{x}_1, \mathbf{x}_2, \dots, \mathbf{x}_n]^\top$ , where each  $\mathbf{x}_i \in \mathbb{R}^d$ , denote the  $n$  input points with corresponding observations  $\mathbf{y} = [y_1, y_2, \dots, y_n]^\top$ . A GP with zero mean and kernel  $K_\theta(\mathbf{x}_i, \mathbf{x}_j)$  is formulated as  $\mathbf{y} \sim \mathcal{N}(\mathbf{0}, \Sigma_\theta)$  and its log-likelihood can be represented as shown in [32]:

$$\ell(\theta; \mathbf{y}) = -\frac{n}{2} \log(2\pi) - \frac{1}{2} \log |\Sigma_\theta| - \frac{1}{2} \mathbf{y}^\top \Sigma_\theta^{-1} \mathbf{y}, \quad (1)$$

where  $|\cdot|$  means determinant,  $\Sigma_\theta \in \mathbb{R}^{n \times n}$  has entries  $[\Sigma_\theta]_{ij} = K_\theta(\mathbf{x}_i, \mathbf{x}_j)$  parameterized by  $\theta$ . For a set of  $n^*$  new input points  $\mathbf{X}^* = [\mathbf{x}_1^*, \mathbf{x}_2^*, \dots, \mathbf{x}_{n^*}^*]^\top$ , we are interested in predicting their corresponding observations  $\mathbf{y}^* = [y_1^*, y_2^*, \dots, y_{n^*}^*]^\top$ . The joint distribution of  $\mathbf{y}$  and  $\mathbf{y}^*$  is assumed to be:

$$\begin{bmatrix} \mathbf{y} \\ \mathbf{y}^* \end{bmatrix} \sim \mathcal{N} \left( \mathbf{0}, \begin{bmatrix} \Sigma_\theta & \Sigma_{\theta,*} \\ \Sigma_{\theta,*}^\top & \Sigma_{\theta,*}^* \end{bmatrix} \right),$$

where  $\Sigma_{\theta,*} \in \mathbb{R}^{n \times n^*}$  contains the covariance matrix between  $\mathbf{X}$  and  $\mathbf{X}^*$ , and  $\Sigma_{\theta,*}^* \in \mathbb{R}^{n^* \times n^*}$  contains the covariances among  $\mathbf{X}^*$ . The conditional distribution of  $\mathbf{y}^*$  given  $\mathbf{y}$  is:

$$p(\mathbf{y}^* | \mathbf{y}) \sim \mathcal{N}(\mu^*, \Sigma^*),$$

where the conditional mean  $\mu^*$  and covariance  $\Sigma^*$  are derived as  $\mu^* = \Sigma_{\theta,*}^\top \Sigma_\theta^{-1} \mathbf{y}$ ,  $\Sigma^* = \Sigma_{\theta,*}^* - \Sigma_{\theta,*}^\top \Sigma_\theta^{-1} \Sigma_{\theta,*}$ . The GPs have computational complexity  $\mathcal{O}(n^3)$  and memory complexity  $\mathcal{O}(n^2)$ , making it infeasible on large scale problems.

#### 4.2 Block Vecchia Method

The BV approximation [30] reduces the computational and memory cost of GPs by partitioning/clustering the dataset into  $bc$  disjoint blocks,  $\{\mathbf{B}_1, \mathbf{B}_2, \dots, \mathbf{B}_{bc}\}$ . After applying a permutation  $\zeta$  to order the blocks, the exact likelihood of  $\mathbf{y}$  becomes:

$$p_\theta(\mathbf{y}) = \prod_{i=1}^{bc} p_\theta(\mathbf{y}_{\mathbf{B}_i^\zeta} | \mathbf{y}_{\mathbf{B}_1^\zeta}, \mathbf{y}_{\mathbf{B}_2^\zeta}, \dots, \mathbf{y}_{\mathbf{B}_{i-1}^\zeta}).$$

The BV method approximates each conditional distribution by replacing each vector with a subset of neighbors  $\mathbf{NN}(\mathbf{B}_i^\zeta)$  by:

$$p_\theta(\mathbf{y}) \approx \prod_{i=1}^{bc} p_\theta(\mathbf{y}_{\mathbf{B}_i^\zeta} | \mathbf{y}_{\mathbf{NN}(\mathbf{B}_i^\zeta)}), \quad (2)$$

where the number of  $\mathbf{NN}(\mathbf{B}_i^\zeta)$  is  $m$  and  $m \ll n$ . The prediction for  $\mathbf{y}^*$  under the BV framework approximates the conditional distribution  $p(\mathbf{y}^* | \mathbf{y})$  by the product of block-level conditional distributions. Given the new blocks  $\{\mathbf{B}_1^*, \dots, \mathbf{B}_{bc}^*\}$  on  $\mathbf{X}^*$ , the predictive distribution is:

$$p_\theta(\mathbf{y}^* | \mathbf{y}) \approx \prod_{j=1}^{bc^*} p_\theta(\mathbf{y}_{\mathbf{B}_j^*} | \mathbf{y}_{\mathbf{NN}(\mathbf{B}_j^*)}), \quad (3)$$

where  $\mathbf{NN}(\mathbf{B}_j^*)$  is the neighbors selected from the  $\mathbf{y}$ . The BV method reduces the computational complexity of the exact GPs from  $\mathcal{O}(n^3)$  to  $\mathcal{O}(bc \cdot m^3)$  and memory complexity from  $\mathcal{O}(n^2)$  to  $\mathcal{O}(bc \cdot m^2)$ . Figure 1 shows the computations involved in the BV algorithm [30], which includes three components, clustering  $\{\mathbf{B}_1, \mathbf{B}_2, \dots, \mathbf{B}_{bc}\}$ , Near-est Neighbor Search (NNS)  $\mathbf{NN}(\mathbf{B}_i^\zeta)$ , and batched GPU computing.

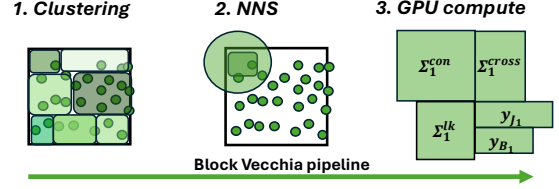


Figure 1: The BV algorithm: (1) disjoint clustering, (2) NNS, and (3) batched GPU log-likelihoods.

#### 4.3 Kullback-Leibler (KL) Divergence

The KL divergence measures how one probability distribution diverges from a second probability distribution [12]. For two Gaussian distributions  $\mathcal{N}_0$  and  $\mathcal{N}_1$  with zero mean and covariance matrices  $\Sigma_0$  and  $\Sigma_1$ , the KL divergence is [29]:

$$D_{KL}(\mathcal{N}_0 \| \mathcal{N}_1) = \frac{1}{2} \left\{ \text{tr}(\Sigma_1^{-1} \Sigma_0) - n + \log \frac{|\Sigma_1|}{|\Sigma_0|} \right\}.$$

For Vecchia-based GPs, previous work [30, 31] shows that the KL divergence simplifies to the difference between exact and approximate log-likelihoods evaluated at  $\mathbf{y} = \mathbf{0}$  as:

$$D_{KL} = \ell_0(\theta; \mathbf{0}) - \ell_a(\theta; \mathbf{0}), \quad (4)$$

where  $\ell_0(\theta; \mathbf{0})$  is the exact log-likelihood and  $\ell_a(\theta; \mathbf{0})$  is Vecchia-based approximated log-likelihood.

This work uses the KL divergence to quantify the discrepancy between the proposed SBV algorithm and posterior distributions from other GP methods.

#### 4.4 Scaled Kernel Function

In high-dimensional spaces, covariance functions often require *anisotropic scaling*, where each input dimension is scaled according to its relevance to the output [24]. This allows the model to reflect varying sensitivities across dimensions and improves both accuracy and efficiency. The scaled covariance function is defined as

$$K_\theta(\mathbf{x}_k, \mathbf{x}_{k'}) = f \left( \left( \sum_{i=1}^d \frac{(x_{ki} - x_{k'i})^2}{\beta_i^2} \right)^{\frac{1}{2}} \right), \quad (5)$$

where  $x_{ki}$  and  $x_{k'i}$  denote the  $i$ -th components of  $\mathbf{x}_k$  and  $\mathbf{x}_{k'}$ , and  $\boldsymbol{\beta} = (\beta_1, \dots, \beta_d)^\top$  contains the dimension-specific range (scaling) parameters.  $f(\cdot)$  is a kernel function, such as the Matérn kernel:

$$f(r) = \sigma^2 \frac{2^{1-\nu}}{\Gamma(\nu)} r^\nu \mathcal{K}_\nu(r) + \sigma_0^2. \quad (6)$$

Here,  $r$  is the scaled distance and  $\theta = (\sigma^2, \boldsymbol{\beta}, \nu, \sigma_0)^\top$  denotes the kernel parameters:  $\sigma^2$  (process variance),  $\sigma_0^2$  (nugget), and  $\nu > 0$  (smoothness).  $\Gamma(\cdot)$  is the gamma function, and  $\mathcal{K}_\nu(\cdot)$  is the modified Bessel function of the second kind of order  $\nu$ . Additional valid covariance classes are detailed in [19]. We use the scaled form in Equation (5) to capture directional relevance, useful in emulation problems where only a subset of input dimensions significantly affect the output.

## 5 Distributed Scaled Block Vecchia Algorithm

This section presents the proposed distributed algorithm, consisting of data preprocessing and batched GPU-based log-likelihood computation. Preprocessing involves input scaling, partitioning, clustering, and NNS. We then analyze the computational complexity of the algorithm, highlighting efficient GPU utilization.

### 5.1 GP Modeling

The distributed SBV algorithm operates through a coordinated workflow across compute nodes, which is detailed in Algorithm 1, and the pipeline is illustrated in Figure 2. The distributed SBV algorithm consists of four key components: scaling and partitioning, Random Anchor Clustering (RAC), filtered subset selection for NNS, and batched GPU computation for optimizing the log-likelihood. The preprocessing steps—scaling and partitioning, RAC, and filtered NNS, are performed only once and executed on the CPU to prepare the data structure. The resulting structured data is then transferred to the GPU, efficiently executing hundreds of parameter optimization iterations without redundant data movement. Steps (2), (3), and (4) are the BV algorithm pipeline.

---

#### Algorithm 1 Distributed SBV approximation algorithm

---

- 1: **Input:** Data  $\{\mathbf{x}_i, y_i\}_{i=1}^n$ , dimension  $d$ , total block count  $K$ , local clusters  $k_p$ , nearest neighbors  $m_{\text{est}}$ , workers  $P$ , covariance function  $K_\theta$ , scaling parameters  $\{\beta_i\}_{i=1}^d$ .
  - 2: **Output:** Approximate the log-likelihood  $\ell$ .
  - 3: **Step 1: Scaling and Partitioning**  $X_p$
  - 4:  $\{X_p; p = 1, 2, \dots, P\} = \mathcal{SP}(X_{1:P})$
  - 5: **Step 2: Random Anchor Clustering**  $B_p$
  - 6:  $\{B_{p,i}; p = 1, 2, \dots, P; i = 1, 2, \dots, k_p\} = \mathcal{C}(X_{1:P})$
  - 7: Randomly reorder these blocks  $B_{p,i}$ ;
  - 8: **Step 3: NNS**  $J_p$
  - 9:  $\{J_{p,i}; p = 1, 2, \dots, P; i = 1, 2, \dots, k_p\} = \mathcal{V}(B_{1:P}, m_{\text{est}})$
  - 10: **Step 4: Batched Log-Likelihood Calculation**  $\log \mathcal{L}_p$
  - 11: **for** each block  $B_p, p = 1, 2, \dots, P$  in Parallel **do**
  - 12:  $\ell_p = \ell_{\text{llh}}(B_p, J_p, \mathbf{y}_{p,B}, \mathbf{y}_{p,J})$ , where  $\mathbf{y}_{p,B}, \mathbf{y}_{p,J}$  is the observations associated with  $B_p$  and  $J_p$  respectively.
  - 13: **end for**
  - 14: **Step 5: Reduction of Log-Likelihood Across Workers**
  - 15: Use MPI\_Allreduce to sum  $\ell_p$  from each worker and obtain the approximated log-likelihood  $\ell$ .
  - 16: **Return:** The approximated log-likelihood  $\ell$ .
- 

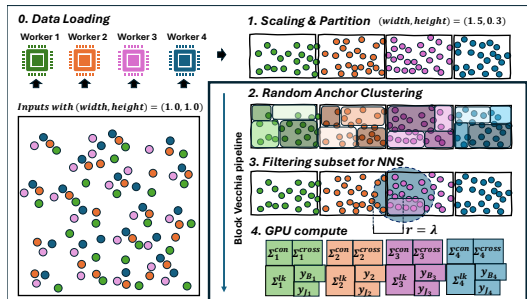


Figure 2: Distributed SBV pipeline.

**5.1.1 Data Scaling and Partitioning.** Each worker  $p$  begins by loading its assigned data subset  $X_p$ , as illustrated in Step 0 of Figure 2. In the case of the synthetic dataset, the dataset is randomly distributed within the unit square  $[0, 1]^2$ , with each color indicating the portion assigned to a specific worker (e.g., four workers in the figure). Input dimensions are then rescaled using anisotropic parameters  $\beta = [\beta_1, \dots, \beta_d]$ . This scaling transforms each dimension  $x_{ij}$  to  $x_{ij} := x_{ij}/\beta_i$ , ensuring that the relevance of different dimensions is appropriately weighted, see line 4 in Algorithm 2. For example, in Step 1 of Figure 2, the input space is rescaled from the unit square to the rectangle  $(0, 1.5) \times (0, 0.3)$ , indicating that the first dimension (width) is more relevant to the response than the second (height). Following the input dimension rescaling, the points are redistributed according to their most relevant dimension, see line 7 in Algorithm 2. Here, the most relevant dimension is denoted by  $d'$ , and MPI\_Alltoall is used to partition the dataset  $X_{1:p}$ , where  $x_{p,i,d'}$  refers to the  $d'$ -th component of the  $i$ -th data point on worker  $p$ . In the example shown in Step 1 of Figure 2, the rescaled input space is partitioned into four segments along the most relevant dimension, with an example scaling factor of  $\beta_2 = 0.3$ . This rescaling and partitioning strategy ensures balanced and uniform data distribution across workers in the algorithm, enhancing computational efficiency while preserving accuracy.

---

#### Algorithm 2 Scaling and Partitioning $\mathcal{SP}(X_{1:P})$

---

- 1: **Input:** Complete dataset  $X_{1:P}$ .
  - 2: **Output:** Scaled and redistributed  $X_{1:P}$ .
  - 3: **for** each worker  $p$  in parallel **do**
  - 4: Scale dimension  $j$  of the local subset  $X_p = \{\mathbf{x}_i \mid i = 1, 2, \dots, n_p\}$ , i.e.,  $x_{ij} := x_{ij}/\beta_j, j = 1, 2, \dots, d$ .
  - 5: **end for**
  - Find the most relevant dimension  $d' = \arg \max_i \{\beta_i, i = 1, 2, \dots, d\}$ .
  - 6: **for** each worker  $p$  in parallel **do**
  - 7: MPI\_Alltoall, redistribute and partition  $x_{p,i}$  according to their  $d'$  dimension, i.e., send  $x_{p,i}$  to  $q$ th node if  $\text{int}(x_{p,i,d'} \times P \times \beta_{d'}) = q$ .
  - 8: **end for**
  - 9: **Return:** Scaled and redistributed  $X_{1:P}$
- 

**5.1.2 Random Anchor Clustering (RAC).** The scaled and partitioned data is then clustered into disjoint blocks  $B_{1:P}$ , where each block is defined as  $B_p := \{B_{p,1}, \dots, B_{p,k_p}\}$ , as outlined in Step 2 of Algorithm 1 and illustrated in Step 2 in Figure 2. The RAC method is detailed in Algorithm 3. Here, we replace the K-means clustering in block Vecchia GPs [31] with RAC to reduce the computational cost induced by K-means for extensive datasets while maintaining comparable approximation accuracy. The RAC algorithm begins by randomly selecting  $k_p$  anchors (centers) for each worker  $p = 1, 2, \dots, P$  in parallel. These anchors serve as the centers of blocks. Subsequently, each  $x_{p,i}$  is assigned to the  $j$ th block based on their distance, as shown in line 5 of Algorithm 3, thus constructing clusters,  $B_p := (B_{p,1}, B_{p,2}, \dots, B_{p,k_p})$  with  $p = 1, 2, \dots, P$ . The RAC method does not involve any communication between workers considering that the size of clusters is typically much smaller than

the overall dataset. For example, a single cluster may contain only 100, while the entire dataset consists of 10 million locations.

---

**Algorithm 3** RAC algorithm  $C(X_{1:P})$ 


---

- 1: **Input:**  $X_{1:P}$  full dataset.
  - 2: **Output:**  $B_{1:P}$  set of cluster for each node.
  - 3: **for** each worker  $p$  in parallel **do**
  - 4: Randomly choose  $k_p$  local centers  $C_p = \{c_{p,i} \mid i = 1, 2, \dots, k_p\}$  in  $X_p$ , and initialize  $B_{p,j} = \{c_{p,i}\}$ .
  - 5: Assign  $\mathbf{x}_{p,i}$  to  $j$ th cluster  $B_{p,j}$ , where  $j = \arg \min_j \|\mathbf{x}_{p,i} - c_{p,j}\|^2, j = 1, 2, \dots, k_p$ .
  - 6: **end for**
  - 7: **Return:** Clusters  $B_{1:P}$
- 

---

**Algorithm 4** NNS algorithm based on filtered subset  $\mathcal{V}(B_p, m)$ 


---

- 1: **Input:**  $B_p$  cluster set, nearest neighbors  $m$ , expansion factor  $\alpha = 100$  (default).
  - 2: **Output:** Nearest neighbor set  $J_{1:P}$
  - 3: **Step1: Distance Threshold and Centers**
  - 4: Calculate distance threshold,  $\lambda$  according to Equation(7).
  - 5: **for** each block  $B_{p,i}$  in  $B_p$  **do**
  - 6: Update centers  $C_i = \{c_{p,i}\}$ , where  $c_{p,i} = \frac{1}{k_{p,i}} \sum_{i=1}^{k_{p,i}} \mathbf{x}_{p,i}$  with  $\mathbf{x}_{p,i} \in B_{p,i}$ .
  - 7: **end for**
  - 8: All\_Gather, gather all centers  $C_{1:P}$  to each worker.
  - 9: **Step 2: Prepare Coarser Candidates**
  - 10: **for** each worker  $p$  in parallel **do**
  - 11: MPI\_Alltoall, redistribute  $B_{p,i}$  to  $q$ th node if  $\|c_{p,i} - c_{q,j}\|^2 \leq \lambda$  where  $j$  exists.
  - 12: Received clusters form the candidate set  $B_p^{cand}$  for worker  $p$ .
  - 13: **end for**
  - 14: **Step 3: Prepare Finer Candidates for NN**
  - 15: **for** local block center  $c_i$  in  $\{c_i\}_{i=1}^{k_p}$  **do**
  - 16: **for** candidate block center  $c_j$  in  $B_p^{cand}$  **do**
  - 17: **if** The order  $c_j$  not exceeds order  $c_i$  **then**
  - 18: **for** each point  $\mathbf{x}_k$  in  $B_{p,j}^{cand}$  **do**
  - 19: Calculate the distance  $d(c_i, \mathbf{x}_k)$ . If  $d(c_i, \mathbf{x}_k) < \lambda$ , add  $\mathbf{x}_k$  to the candidate set  $S_{p,i}$  for block  $B_{p,i}$ .
  - 20: **end for**
  - 21: **end if**
  - 22: **end for**
  - 23: Searching  $m$  nearest neighbors for  $i$ th block, i.e.,  $J_{p,i} = \text{NNS}(c_i, S_{p,i}, m)$ .
  - 24: **end for**
  - 25: **Return:** Nearest neighbor set  $\{J_p, p = 1, 2, \dots, P\}$ .
- 

**5.1.3 Filtered  $m$ -Nearest Neighbor Search (NNS).** With block sets  $B_{1:P}$ , the next goal is to find the exact  $m$  nearest neighbors for all block centers, where search areas are varied for each query center in the Vecchia-based GPs, see Equation (2). Existing methods [1, 11, 16] for exact  $m$ -NNS with query-specific search areas face limitations, especially for large datasets.

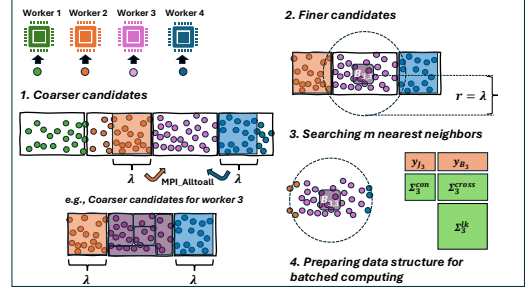


**Figure 3: Filtered NNS algorithm pipeline.**

To address these issues, we adopt the filtered  $m$ -NNS on each block  $B_{p,i}$ , as illustrated in Step 3 of Figure 2. This approach selects a small filtered subset (a circle of radius  $\lambda$ ) for brute-force  $m$ -NNS to obtain exact results while reducing computational cost. In Algorithms 1 and 4,  $\mathcal{V}$  denotes the filtered  $m$ -NNS function, which begins by computing a Monte Carlo-based distance threshold. This threshold  $\lambda$  is calculated using:

$$\lambda = \left( \alpha \frac{m\zeta}{n} \right)^{1/d}, \quad \zeta = \begin{cases} \frac{\Gamma(\frac{d}{2}+1)}{2\pi^{\frac{d}{2}-1} \Gamma(\frac{d+1}{2})} & d \text{ is even} \\ \frac{\pi^{\frac{d}{2}}}{\Gamma(d+1)} & d \text{ is odd} \end{cases}. \quad (7)$$

Here,  $n$  is the total number of points,  $m$  is the number of nearest neighbors,  $d$  is the dimensionality, and  $\alpha$  is an expansion factor to account for irregularities in point distribution (e.g.,  $\alpha = 100$  implies the candidate set is expected to be 100 times larger than  $m$ ). Then, we prepare the small filtered subset, which consists of two steps, *coarser* and *finer* preparation. In the *coarser* preparation, each worker redistributes candidate clusters to the corresponding worker if the distance between two centers is within the calculated threshold using MPI\_Alltoall. The complementary coarser candidate set is denoted as  $B_p^{cand}$  (lines 10-13 in Algorithm 4). In the *finer* partition, each worker independently selects finer candidates  $S_{p,i}$  for the  $i$ th cluster, i.e.,  $\mathbf{x}_k$  is added to the finer candidate set  $S_{p,i}$  if the distance between the  $i$ th local center and the data point  $\mathbf{x}_k$  is within the threshold  $\lambda$  (lines 15-22 in Algorithm 4). Finally, each local center  $c_i$  applies brute-force search for its  $m$  nearest neighbors  $J_{p,i}$  from the finer candidates set  $S_{p,i}$ . The computational cost of brute search in  $S_{p,i}$  is negligible compared to  $O(n)$  due to  $\alpha m \ll n$  and total block count  $K \ll n$ , thus filtered  $m$ -NNS achieves computational complexity  $O(\alpha m + K)$  and has a simple implementation. Figure 3 illustrates the filtered  $m$ -NNS using an example of four workers. In the coarser candidate preparation, MPI\_Alltoall is utilized to distribute related blocks (within distance threshold  $\lambda$ ) to the 3rd worker, forming the coarse candidates  $B_3^{cand}$ . Subsequently, the 3rd block  $B_{3,3}$  refines candidates for the brute  $m$ -NNS (within distance threshold  $\lambda$ ). Finally, blocks with their nearest neighbors and their observations are constructed as the contiguous arrangement for batched GPU computing.

**5.1.4 Batched Log-likelihood Computations.** Once the data preprocessing is finished, we copy clusters  $B_{1:P}$ , nearest neighbors  $J_{1:P}$ , and their observations to GPU global memory for log-likelihood optimization. Algorithm 5 outlines the computation of a single iteration of log-likelihood, which needs to be evaluated multiple times



until the prespecified optimization configuration is achieved. Here, the batched operations execute for log-likelihood computation. This involves constructing local covariance matrices  $\Sigma^{lk}$ ,  $\Sigma^{cross}$  and  $\Sigma^{con}$  using the scaled kernel  $K_\theta$ . Subsequently, the GPU data structure is constructed in Step 4 in Figure 2. Following, batched Cholesky decompositions (POTRF) is utilized to factorize neighbor covariance matrices,  $\Sigma^{con}$ . Conditional mean and covariance updates are computed via batched triangular solver (TRSM) and matrix multiplications (GEMM), while batched triangular solver (TRSV) and determinant calculations derive per-block log-likelihoods  $\ell_{p,i}$ . Each node aggregates its local computations  $\ell_p = \sum_{i=1}^{k_p} \ell_{p,i}$ , and a global reduction across all nodes yields the final log-likelihood  $\ell = \sum_{p=1}^P \ell_p$  using MPI\_Allreduce.

---

**Algorithm 5** Batched Block Vecchia  $\ell_{llh}(B_p, J_p, \mathbf{y}_{p,B}, \mathbf{y}_{p,J})$ 


---

```

1: Input: In  $p$ th node,  $B_p$  cluster set,  $J_p$  nearest neighbor set,  $\mathbf{y}_{p,B}$ 
   and  $\mathbf{y}_{p,J}$  observation sets.
2: Output: log-likelihood  $\ell_p$ 
3: Step 1: Conditional Mean and Covariance Update
4:  $\Sigma^{lk} \leftarrow \text{batched } K_\theta(B_p, B_p)$ .
5:  $\Sigma^{con} \leftarrow \text{batched } K_\theta(J_p, J_p)$ .
6:  $\Sigma^{cross} \leftarrow \text{batched } K_\theta(J_p, B_p)$ .
7:  $L \leftarrow \text{batched POTRF}(\Sigma^{con})$ 
8:  $\Sigma'^{cross} \leftarrow \text{batched TRSM}(L, \Sigma^{cross})$ 
9:  $\mathbf{y}'_{p,J} \leftarrow \text{batched TRSV}(L, \mathbf{y}_{p,J})$ 
10:  $\Sigma^{cor} \leftarrow \text{batched GEMM}(\text{transpose}(\Sigma'^{cross}), \Sigma'^{cross})$ 
11:  $\boldsymbol{\mu}^{cor} \leftarrow \text{batched GEMV}(\text{transpose}(\Sigma'^{cross}), \mathbf{y}'_{p,J})$ 
12:  $\Sigma^{new} \leftarrow \Sigma^{con} - \Sigma^{cor}$ 
13:  $\boldsymbol{\mu}^{new} \leftarrow \boldsymbol{\mu}^{cor}$ 
14: Step 2: GPs calculations
15:  $L' \leftarrow \text{batched POTRF}(\Sigma^{new})$ 
16:  $\mathbf{v} \leftarrow \text{batched TRSV}(L', \mathbf{y}_{p,B} - \boldsymbol{\mu}^{new})$ 
17:  $\mathbf{u} \leftarrow \text{batched DotProduct}(\text{transpose}(\mathbf{v}), \mathbf{v})$ 
18:  $\mathbf{d} \leftarrow 2 \times \log(\text{determinant}(L'))$ 
19:  $\ell_p \leftarrow -\frac{1}{2} \mathbf{1}^T (\mathbf{u} + \mathbf{d})$ 
20: return log-likelihood  $\ell_p$ 

```

---

**5.1.5 GP Prediction.** During the prediction stage, the pipeline closely follows the estimation process, with the key difference being that in Step (2) GP calculations in Algorithm 5 are replaced by conditional simulations. Specifically, the variance vector,  $\boldsymbol{\sigma} = (\sigma_1, \sigma_2, \dots, \sigma_{n^*})^T$  is subtracted from the diagonal elements of the covariance matrices  $\Sigma^{new}$ , and  $\boldsymbol{\mu}^{new}$  serves as the predicted values,  $(y_{*1}, y_{*1}, \dots, y_{*n^*})$ . Next, conditional simulations are performed by drawing 1000 samples from the normal distribution  $\mathcal{N}(y_{*j}, \sigma_j)$ . Then, the sample mean  $\tilde{\mu}_j$  and variance  $\tilde{\sigma}_j^2$  are computed, and the 95% confidence interval is given by,  $(\tilde{\mu}_j - z_{\alpha/2} \tilde{\sigma}_j, \tilde{\mu}_j + z_{\alpha/2} \tilde{\sigma}_j)$ , where  $\alpha = 0.05$ ,  $j = 1, 2, \dots, n^*$ , which follows the same as [31].

Overall, the workflow minimizes inter-node communication and computations by scaling and partitioning, RAC, and filtered  $m$ -NNS, while GPU-batched kernels exploit fine-grained parallelism for covariance and log-likelihood computations. Moreover, this algorithm incorporates anisotropic scaling for high-dimensional inputs to ensure accurate emulation for computer models. This

framework enables scalable and efficient log-likelihood evaluation for large-scale GPs in the high-dimensional problem setup.

## 5.2 Complexity Analysis

We analyze the memory and computational complexity of SV and SBV, focusing on the estimation of GPU stage, which dominates due to repeated iterations, unlike the one-time CPU preprocessing.

For SV, the memory footprint is  $O(nm^2 + nm)$ , primarily due to the storage of  $n$  small covariance matrices  $\Sigma_{1:n}$  and corresponding conditioning vectors  $\mathbf{y}_{1:n}$ . In contrast, SBV partitions the data into  $bc$  blocks. Each block stores three covariance matrices, i.e.,  $\Sigma_i^{lk}$ ,  $\Sigma_i^{cross}$ , and  $\Sigma_i^{con}$ , and two observation vectors:  $\mathbf{y}_{J_i}$  for the conditioning set and  $\mathbf{y}_{B_i}$  for the block itself. Assuming an average block size of  $bs = n/bc$ , the memory complexity for each SBV component is:  $O(n \cdot bs)$  for  $\Sigma_i^{lk}$ ,  $O(mn)$  for  $\Sigma_i^{cross}$ ,  $O(bc \cdot m^2)$  for  $\Sigma_i^{con}$ ,  $O(bc \cdot m)$  for  $\mathbf{y}_{J_i}$ , and  $O(n)$  for  $\mathbf{y}_{B_i}$ . Therefore, the total memory complexity is  $O(nm^2 + nm)$  for SV and  $O(n \cdot bs + mn + bc \cdot m^2)$  for SBV.

The dominant computational costs in SBV arise from Cholesky factorizations and matrix-matrix multiplications. The Cholesky operations contribute  $O(bc \cdot bs^3)$  for block matrices and  $O(bc \cdot m^3)$  for the conditioning sets. Matrix-matrix multiplications add a complexity of  $O(mn \cdot bs)$ . Thus, the total computational complexity for SBV is  $O(n \cdot bs^2 + bc \cdot m^3 + mn \cdot bs)$ , compared to  $O(nm^3)$  for SV, which performs a Cholesky factorization for each data point.

For high-dimensional input spaces, we recommend setting the number of nearest neighbors to four times the block size, i.e.,  $m = 4 \times bs$ . Under this setting, the complexities simplify and are summarized in Table 2. SBV achieves lower memory and computational costs than SV, especially when leveraging GPU-batched operations for large-scale GP models.

**Table 2: Complexity analysis for SV and SBV under  $m = 4 \times bs$ .**

Method	Memory	Computational
SV	$O(nm^2)$	$O(nm^3)$
SBV	$O(nm)$	$O(nm^2)$

## 6 Simulation and Benchmark Evaluation

This section begins with a synthetic GP simulation using the Matérn kernel in high-dimensional input space, highlighting the critical role of scaling and clustering. We then apply the proposed SBV algorithm to the satellite drag benchmark dataset to demonstrate its effectiveness and accuracy in emulating complex computer models.

### 6.1 Synthetic Data Simulation

The simulation framework follows the design outlined in [24], ensuring consistency for comparative analysis. The synthetic dataset is generated from a zero-mean GP with a Matérn kernel ( $\nu = 3.5$ ) using Equation (6). The input space is,  $\mathbf{x} \in [0, 1]^{10}$ . The response is modeled as  $\mathbf{y}(\mathbf{x}) \sim \mathcal{N}(\mathbf{0}, K_\theta(\mathbf{x}, \mathbf{x}'))$ , where the parameter vector is given by  $\boldsymbol{\theta} = (\sigma^2, \tau^2, \boldsymbol{\beta})$ . The true parameters are set as  $(\sigma^2, \tau^2) = (1.0, 0)$ , with range parameters  $\beta_1 = \beta_2 = 0.05$  for the relevant dimensions and  $\beta_3 = \beta_4 = \dots = \beta_{10} = 5$  for the irrelevant ones. We evaluate four Vecchia-based GPs on this synthetic dataset: CV [40], BV [31], SV [24], and our proposed SBV. The choice of

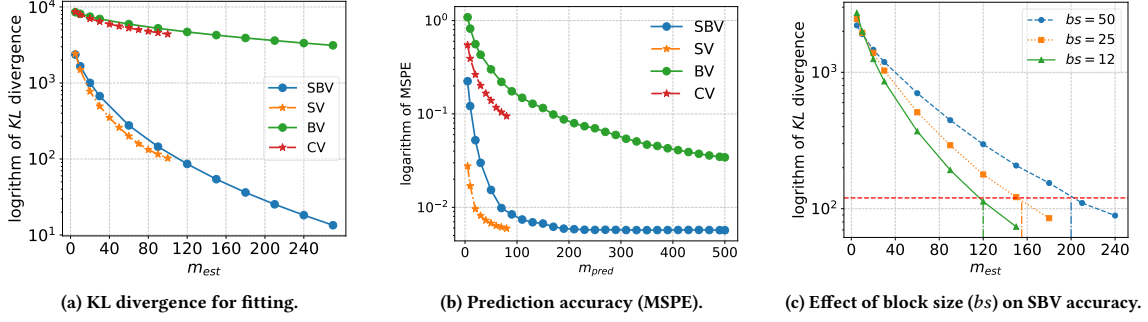


Figure 4: Comparison of Vecchia-based GP methods on model fitting and prediction accuracy.

$bs_{est} = bs_{pred} = 10$  in BV and SBV reflects a balance between computational efficiency and predictive accuracy. Model performance is assessed using both the KL divergence defined in Equation (4) and the Mean Squared Prediction Error (MSPE). To isolate approximation error and avoid conflating it with parameter estimation error, the true parameters ( $\sigma^2$ ,  $\tau^2$ ,  $\beta$ ) are directly supplied to all four models.

The results are presented in Figure 4. In Figure 4a, the proposed SBV method achieves the lowest KL divergence, followed by SV, BV, and CV, highlighting the advantage of combining input scaling and clustering over the CV approach. The performance gains of SBV arise from its ability to address input anisotropy through joint scaling and to increase neighborhood coverage through clustering. Figure 4b shows a similar trend regarding predictive accuracy, where SBV again yields the lowest MSPE, followed by SV, BV, and CV. These results are consistent with the KL divergence findings and further validate the benefits of incorporating input scaling and structured clustering. In Figure 4c, we examine the impact of block size on KL divergence. Smaller blocks ( $bs_{est} = 12$ ) result in lower KL divergence compared to larger ones ( $bs_{est} = 50$ ), indicating improved approximation accuracy with finer partitioning. However, larger blocks impose heavier computational loads, which in turn allow for more effective GPU utilization. Therefore, the choice of block size  $bs$  introduces a trade-off between accuracy and computational cost.

## 6.2 Evaluation on Satellite Drag Benchmark

The satellite drag dataset from [39] is a widely used benchmark for evaluating GP-based models in high-dimensional settings [24, 39]. It is generated from a high-fidelity simulator that models atmospheric drag coefficients in low Earth orbit (LEO). The dataset comprises 2M simulation runs for each of six primary atmospheric species: atomic oxygen (O), molecular oxygen ( $O_2$ ), atomic nitrogen (N), molecular nitrogen ( $N_2$ ), helium (He), and atomic hydrogen (H). The total drag coefficient is computed as a weighted average of these species. Each species-specific dataset has an 8-dimension input space: relative velocity, surface temperature, atmospheric temperature, yaw angle, pitch angle, and two accommodation coefficients [39].

Following the experimental design in [24], we split the dataset into 90% for training and 10% for testing and performed 10-fold cross-validation for robust evaluation. We adopt the same Matérn

kernel with nugget effects, and smoothness parameter  $\nu = 3.5$  as in [24]. Model performance is assessed using the Root Mean Squared Percentage Error (RMSPE) and the estimated kernel parameters. The models compared in this study are mentioned in Table 3.

Table 3: Vecchia-based GP configurations on the satellite drag dataset, showing block sizes ( $bs_{est}$ ,  $bs_{pred}$ ) and neighbor counts ( $m_{est}$ ,  $m_{pred}$ ) for estimation and prediction.

Model	SV	SBV <sub>1</sub>	SBV <sub>2</sub>	SBV <sub>3</sub>	SBV <sub>4</sub>	SBV <sub>5</sub>	SBV <sub>6</sub>
$bs_{est}$	1	100	100	100	100	100	100
$bs_{pred}$	1	5	5	5	5	5	5
$m_{est}$	50	200	200	200	400	400	400
$m_{pred}$	140	200	400	600	200	400	600

For model fitting, SV uses  $m_{est} = 50$  nearest neighbors on a 50K-sample subset, following the configuration in [24], which reported only marginal gains in predictive accuracy beyond this setting relative to the increased computational cost. In contrast, SBV leverages the full dataset with larger neighbor counts ( $m_{est} = 200$  or  $400$ ) while maintaining a consistent average block size of  $bs_{est} = 100$  across all configurations. Due to the high memory and computational demands of SV, fitting the full dataset on a single GPU is infeasible, making SBV a more practical and scalable alternative.

Figure 5 presents the RMSPE results for Vecchia-based GP models on the benchmark dataset. SBV consistently achieves the lowest RMSPE, demonstrating the effectiveness of combining input scaling with clustering. Increasing the number of prediction neighbors  $m_{pred}$  improves accuracy; for example, SBV with  $m_{pred} = 400$  reduces RMSPE by approximately 15% on average compared to  $m_{pred} = 200$ . To better understand the improved accuracy achieved by SBV, Figure 6 compares the estimated inverse lengthscales ( $1/\beta_i$ ) for SV and SBV. Both methods identify the final three input dimensions as most relevant while treating the others as less influential. However, the parameter estimates produced by SBV differ significantly from those of SV, underscoring the importance of using a larger number of nearest neighbors for accurate GP fitting. From a computational and memory perspective, SV faces challenges in handling large neighbor counts due to substantial cost and memory usage increases, which limits efficient GPU utilization. In contrast, SBV remains scalable and efficient under these conditions.

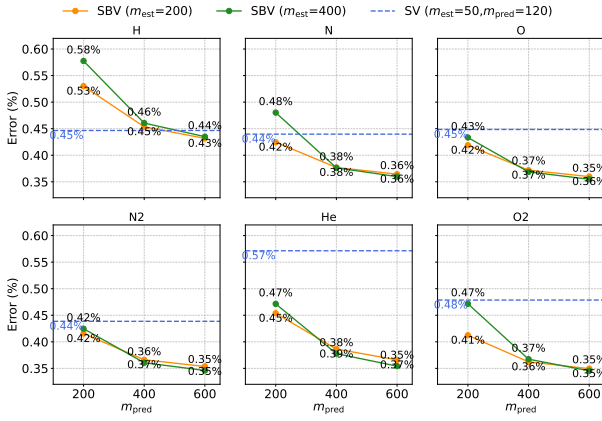


Figure 5: RMSPE of Vecchia-based GP models on six outputs from the satellite drag benchmark.

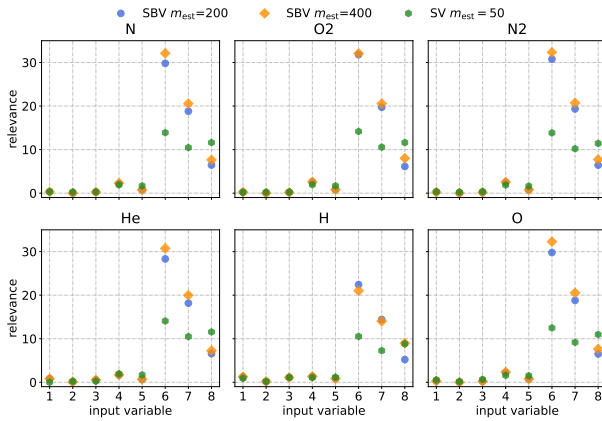


Figure 6: Estimated input relevance ( $1/\beta_i$ ) for SV and SBV on the satellite drag benchmark.

### 6.3 MetaRVM Emulator

MetaRVM [15] is an R package that simulates the spread of respiratory viruses using a graph-based probabilistic model. By dividing a total population into sub-populations such as zones, age groups, or races, it models disease dynamics within and between these groups. This structure allows for the simulation of interactions and disease spread both within and between sub-populations. In healthcare, such models are crucial for understanding transmission patterns, evaluating intervention strategies, and informing public health policies. They help predict outbreak trajectories, assess the potential impact of vaccinations, and optimize resource allocation, ultimately aiding in the control and prevention of respiratory infections. The parameters in MetaRVM simulator are listed in Table 4. To understand the relationship between the input parameters and the accumulated number of hospitalizations (output) over 100 days in one population, we randomly choose 50M sets of input variables and obtain the accumulated hospitalizations using MetaRVM simulator. The 50M outputs are then divided into 90% for fitting SBV GPs with Matérn kernel at  $\nu = 3.5$  and 10% is used for prediction

where the RMSPE is reported. Additionally, the input is scaled into  $[0, 1]$ , and the output is normalized with mean 1 to avoid the abnormal values in RMSPE. In the SBV, we set  $bs_{est} = 100$ ,  $bs_{pred} = 25$  and investigate the accuracy as increasing the number of nearest neighbors.

Table 4: The MetaRVM dataset simulation parameters.

Input	Meaning	Bound
$ts$	transmissibility for susceptible	(0.1, 0.9)
$tv$	transmissibility for vaccinated	(0.1, 0.9)
$dv$	mean duration in vaccinated state	(30, 90)
$de$	mean duration in exposed state	(1, 5)
$dp$	mean duration in infectious presymptomatic state	(1, 3)
$da$	mean duration in infectious asymptomatic state	(1, 9)
$ds$	mean duration in infectious symptomatic state	(1, 9)
$dh$	mean duration in hospitalized state	(1, 5)
$dr$	mean duration in recovered state	(30, 90)
$ve$	vaccine efficacy	(0.3, 0.8)

The results are presented in Figure 7, where a large  $m$  for both estimation and prediction generally leads to improved RMSPE. In the parameter estimation, the relevance  $dh$  and  $dr$  is close to 0, which aligns with our expectation, as these parameters are not involved in the accumulated number of hospitalizations in the MetaRVM simulator. Besides, for  $ds$  and  $tv$ , the estimation varies significantly to the increasing value of  $m_{est}$ .

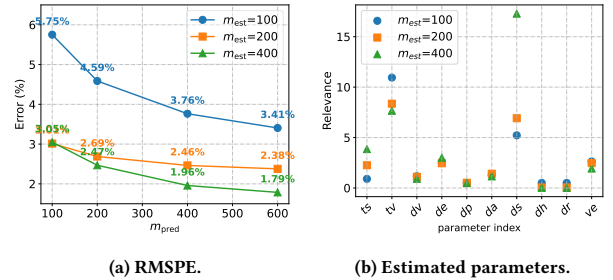
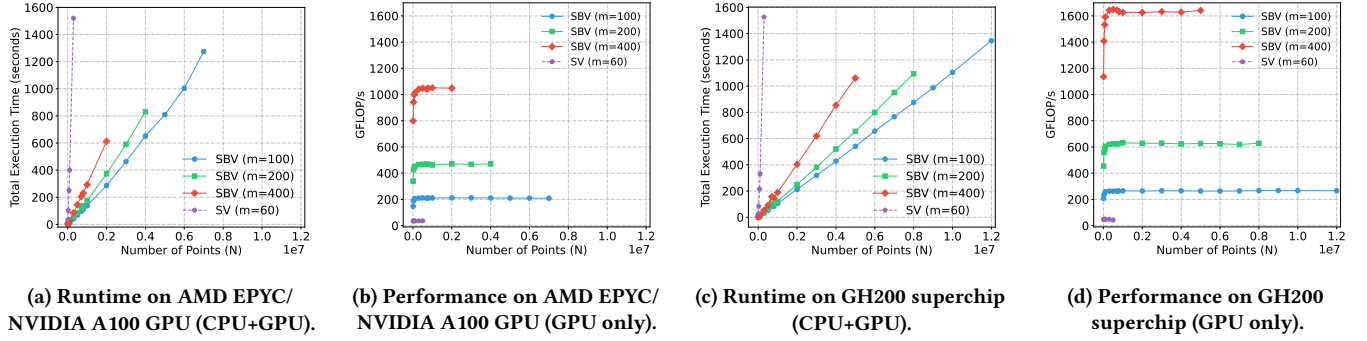


Figure 7: Accuracy of SBV algorithm on MetaRVM dataset.

## 7 Performance and Energy Evaluation

We conduct experiments on two modern NVIDIA GPU architectures, A100 and GH200, hosted at the Jülich Supercomputing Centre (JSC) on the JURECA-DC GPU and JEDI systems. JEDI, a development platform for the upcoming JUPITER exascale system, features 48 nodes, each equipped with four NVIDIA GH200 Grace Hopper Superchips. Each Superchip integrates a 72-core Grace CPU (3.1 GHz, 120 GB) and a Hopper GPU (96 GB HBM3), connected via NVLink-C2C (900 GB/s), with a total power consumption of approximately 680 W per Superchip. JURECA-DC GPU comprises 192 nodes, each with two 64-core AMD EPYC 7742 CPUs (2.25 GHz, 512 GB, 225 W per socket) and four NVIDIA A100 GPUs (40 GB HBM2, 400 W per GPU). Both systems use InfiniBand interconnects: JEDI provides four NDR200 (200 Gbit/s) links per node, while JURECA-DC GPU offers two HDR (200 Gbit/s) links per node. Our





**Figure 8: Performance comparison of SBV and SV methods with 500 MLE iterations on single AMD EPYC with NVIDIA A100 (40 GB) and single NVIDIA GH200 superchip (96 GB).**

framework is compiled with GCC 13.3.0, uses CUDA 11.8/12.0, and links against MAGMA 2.7.2 and NLOpt 2.7.1.

### 7.1 Single-Node Performance

Figure 8 illustrates the runtime and GPU throughput performance of the SBV and SV methods on two nodes: an NVIDIA A100 with its host CPU, and the GH200 Superchip. Subfigures (a) and (c) show that SBV consistently outperforms SV in total execution time across different values of  $m$ , demonstrating superior scalability as the dataset size increases. As expected, larger values of  $m$  increase the total runtime due to higher computational cost per iteration; however, they also lead to significantly better approximation and prediction accuracy, as shown in the accuracy section.

Subfigures (b) and (d) highlight the GPU throughput (in GFLOP/s) for a single iteration, showing that SBV achieves significantly higher sustained performance than SV on both platforms. Notably, the GH200 delivers peak throughput exceeding 1600 GFLOP/s with  $m = 400$ , indicating the benefit of deep integration between the Grace CPU and Hopper GPU. These results confirm that SBV is faster and more GPU-efficient than SV, particularly when leveraging larger neighborhoods on modern architectures like the GH200.

### 7.2 Scalability Across Multiple Nodes

Figure 9 demonstrates the weak and strong scaling performance of the distributed SBV implementation on NVIDIA A100 and GH200 architectures, scaling up to 64 GPUs. In weak scaling (Subfigures (a) and (c)), both systems maintain high parallel efficiency ( $PE$ ) as the problem size increases proportionally with the number of GPUs, with GH200 showing better balance due to its high memory bandwidth and unified Grace-Hopper architecture. In strong scaling (Subfigures (b) and (d)), total execution time decreases nearly linearly with increasing GPU count, and parallel efficiency exceeds ideal scaling ( $PE > 1.0$ ) in several cases due to improved GPU occupancy and kernel batching. The influence of neighborhood size  $m_{est}$  is also evident: larger values such as  $m = 400$  increase the computational workload per point and runtime but result in better GPU throughput and overall hardware utilization. Smaller values, such as  $m = 100$ , lead to faster runtimes but less efficient GPU use, especially on GH200. Mid-range values (e.g.,  $m = 200$ ) balance performance and efficiency.

A detailed breakdown shows that GPU compute time dominates execution, accounting for over 85% of the total runtime in large problem sizes. However, the remaining CPU-side computation introduces variations in scaling. On A100, limited CPU resources (32 cores per task) contribute to a gradual drop in  $PE$ , while the 72-core CPU on GH200 helps better hide this overhead. This difference comes from the role of the CPU in maintaining a globally sorted array for block reordering and candidate filtering, as in Equation (2).

In strong scaling, both platforms exhibit slight fluctuations in  $PE$  attributed to the fixed distance threshold parameter  $\alpha = 500$  used in the filtered NNS, see Equation (7). This value is empirically chosen to guarantee sufficient candidates per block under typical random input settings, up to 5M points on GH200 and 2M on A100. However, as the number of GPUs increases, the candidate count does not scale proportionally and retains some stochastic variability, introducing non-uniform load balancing across tasks. SBV demonstrates excellent scalability up to 64 GPUs across both architectures, with GH200 achieving higher efficiency and better performance at all scales and neighborhood sizes.

### 7.3 Power Consumption Analysis

Figure 10 presents the power consumption profiles of a single A100 and GH200 superchip GPU while running 500 log-likelihood iterations across varying neighborhood sizes ( $m_{est}$ ), using a problem size of 2M points on A100 and 5M on GH200, the largest size that fits in GPU memory. As expected, both power draw and total energy consumption increase with larger  $m_{est}$  due to the higher computational workload. On A100 (Figure 10a), power remains well below the 400 W limit, with total energy ranging from 38.4 kJ ( $m_{est} = 100$ ) to 142.2 kJ ( $m_{est} = 400$ ). In contrast, the Hopper GPUs as part of the GH200 superchips (Figure 10b) consume significantly more energy, up to 343.4 kJ, while handling a larger problem size, enabled by a higher power envelope. For GH200 superchips, the maximum power consumption is per superchip (680 W for each GH200 in JEDI) and the Grace CPU is prioritized. To avoid power shortage and thus performance drops of the Hopper GPUs, the maximum CPU power consumption can be capped (including RAM and system I/O). On the JEDI system, the default CPU power cap is 100 W leaving at least 580 W for the Hopper GPUs. The figure also shows that the GH200 exhibits smoother power traces across all

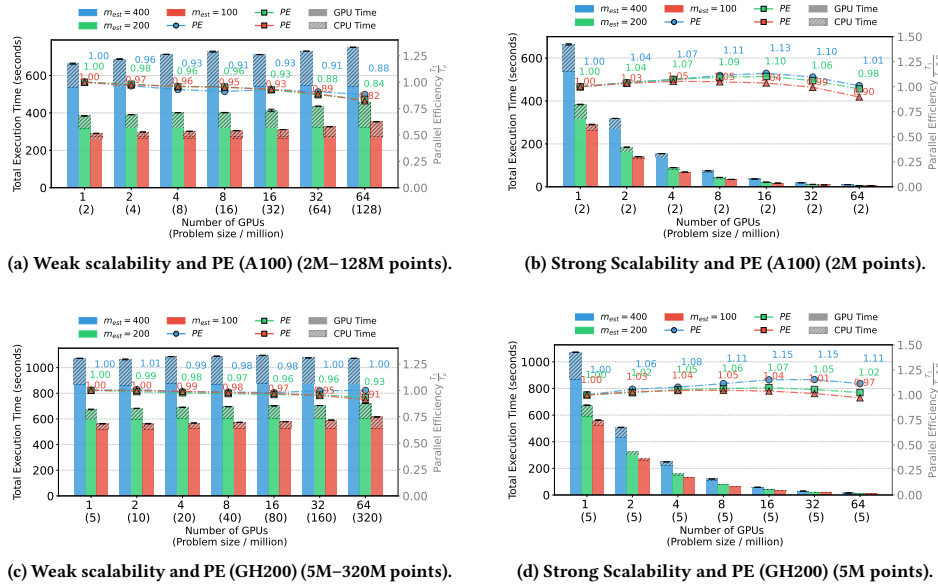


**Figure 9: Weak and strong scaling of SBV were evaluated on up to 64 GPUs, using 500 MLE iterations on two architectures: AMD EPYC with NVIDIA A100 (40 GB, up to 128M points) and the NVIDIA GH200 superchip (96 GB, up to 320M points).**

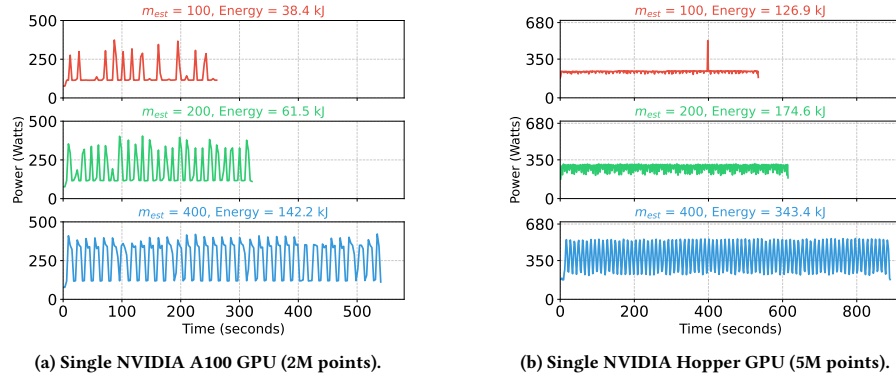


**Figure 10: Power consumption/energy (kJ) on a single GPU for two NVIDIA GPUs over 500 iterations per  $m_{est}$ . A100 GPU with 400 W max power cap and Hopper GPU with <680 W - the power usage of the Grace CPU, RAM, and system I/O> max power cap.**

$m_{est}$  values, indicating stable GPU occupancy, while A100 shows periodic bursts at smaller  $m_{est}$ , reflecting irregular utilization.

We also compare our results to the power profiles of exact GPs reported in [10], which measure the energy consumption of Cholesky-based FP64 and exact GP variants on V100, A100, and H100 GPUs. In that study, a single MLE iteration exceeds 140 kJ on A100 and 340 kJ on H100, even for relatively small matrix sizes (122,880 points). In contrast, our full SBV-based MLE estimation—which includes 500 iterations on much larger datasets (2M and 5M points)—consumes only ~12–40% of the energy required for a single exact GP iteration on those systems, despite handling problems that are 16× to 40× larger. These results highlight the energy efficiency of SBV on modern GPU architectures such as GH200 while demonstrating its scalability for high-dimensional, large-scale GP modeling.

## 8 Conclusion

This paper introduced the Scaled Block Vecchia (SBV) approximation, a novel framework for scalable GP emulation tailored for high-dimensional datasets on distributed GPU systems. By integrating anisotropic input scaling with block-based conditioning and leveraging batched GPU kernels, SBV substantially reduces memory and computational costs while maintaining high predictive accuracy. To our knowledge, this is the first distributed implementation of a Vecchia-based GP approximation. Through extensive experiments on synthetic and real-world data, including the satellite drag benchmark and MetaRVM epidemiological model, we demonstrate the scalability up to 64 GPUs and the ability to handle up to 320M points with energy efficiency and state-of-the-art accuracy.

## References

- [1] Mohammad Reza Abbasifard, Bijan Ghahremani, and Hassan Naderi. 2014. A survey on nearest neighbor search methods. *International Journal of Computer Applications* 95, 25 (2014).
- [2] Sameh Abdulah, Allison H Baker, George Bosilca, Qinglei Cao, Stefano Castruccio, Marc G Genton, David E Keyes, Zubair Khalid, Hatem Ltaief, Yan Song, et al. 2024. Boosting earth system model outputs and saving petabytes in their storage using exascale climate emulators. In *SC24: International Conference for High Performance Computing, Networking, Storage and Analysis*. IEEE, 1–12.
- [3] Sameh Abdulah, Qinglei Cao, Yu Pei, George Bosilca, Jack Dongarra, Marc G Genton, David E Keyes, Hatem Ltaief, and Ying Sun. 2021. Accelerating geostatistical modeling and prediction with mixed-precision computations: A high-productivity approach with PaRSEC. *IEEE Transactions on Parallel and Distributed Systems* 33, 4 (2021), 964–976.
- [4] Sameh Abdulah, Hatem Ltaief, Ying Sun, Marc G Genton, and David E Keyes. 2018. ExaGeoStat: A high performance unified software for geostatistics on manycore systems. *IEEE Transactions on Parallel and Distributed Systems* 29, 12 (2018), 2771–2784.
- [5] Sameh Abdulah, Hatem Ltaief, Ying Sun, Marc G Genton, and David E Keyes. 2018. Parallel approximation of the maximum likelihood estimation for the prediction of large-scale geostatistics simulations. In *2018 IEEE international conference on cluster computing (CLUSTER)*. IEEE, 98–108.
- [6] Sameh Abdulah, Hatem Ltaief, Ying Sun, Marc G Genton, and David E Keyes. 2019. Geostatistical modeling and prediction using mixed precision tile Cholesky factorization. In *2019 IEEE 26th international conference on high performance computing, data, and analytics (HiPC)*. IEEE, 152–162.
- [7] Ioannis Andrianakis and Peter G Challenor. 2012. The effect of the nugget on Gaussian process emulators of computer models. *Computational Statistics & Data Analysis* 56, 12 (2012), 4215–4228.
- [8] Moreno Bevilacqua, Alessandro Fassò, Carlo Gaetan, Emilio Porcu, and Daira Velandia. 2016. Covariance tapering for multivariate Gaussian random fields estimation. *Statistical Methods & Applications* 25 (2016), 21–37.
- [9] T Børvik, OS Hopperstad, T Berstad, and M Langseth. 2001. A computational model of viscoplasticity and ductile damage for impact and penetration. *European Journal of Mechanics-A/Solids* 20, 5 (2001), 685–712.
- [10] Qinglei Cao, Sameh Abdulah, Hatem Ltaief, Marc G Genton, David Keyes, and George Bosilca. 2023. Reducing data motion and energy consumption of geospatial modeling applications using automated precision conversion. In *2023 IEEE International Conference on Cluster Computing (CLUSTER)*. IEEE, 330–342.
- [11] Kenneth L Clarkson et al. 2006. Nearest-neighbor searching and metric space dimensions. *Nearest-neighbor methods for learning and vision: theory and practice* (2006), 15–59.
- [12] Thomas M Cover and Joy A Thomas. 2006. *Elements of Information Theory*. Wiley-Interscience.
- [13] Veronika Eyring, Sandrine Bony, Gerald A Meehl, Catherine A Senior, Bjorn Stevens, Ronald J Stouffer, and Karl E Taylor. 2016. Overview of the Coupled Model Intercomparison Project Phase 6 (CMIP6) experimental design and organization. *Geoscientific Model Development* 9, 5 (2016), 1937–1958.
- [14] Arindam Fadikar, Dave Higdon, Jiangzhuo Chen, Bryan Lewis, Srinivasan Venktraman, and Madhav Marathe. 2018. Calibrating a stochastic, agent-based model using quantile-based emulation. *SIAM/ASA Journal on Uncertainty Quantification* 6, 4 (2018), 1685–1706.
- [15] Arindam Fadikar and Charles Macal. 2025. MetaRVM: Compartmental Model Simulation for Generic Respiratory Virus Diseases. <https://github.com/NSF-RESUME/MetaRVM>. Accessed: April 4, 2025.
- [16] Hakan Ferhatosmanoglu, Ioanna Stanoi, Divyakant Agrawal, and Amr El Abbadi. 2001. Constrained nearest neighbor queries. In *International Symposium on Spatial and Temporal Databases*. Springer, 257–276.
- [17] Sandro Fiore, Mohamed Bakhouya, and Waleed W Smari. 2018. On the road to exascale: Advances in High Performance Computing and Simulations—An overview and editorial. 450–458 pages.
- [18] Reinhard Furrer, Marc G Genton, and Douglas Nychka. 2006. Covariance tapering for interpolation of large spatial datasets. *Journal of Computational and Graphical Statistics* 15, 3 (2006), 502–523.
- [19] Marc G Genton. 2001. Classes of kernels for machine learning: a statistics perspective. *Journal of Machine Learning Research* 2, Dec (2001), 299–312.
- [20] Joseph Guinness. 2018. Permutation and grouping methods for sharpening Gaussian process approximations. *Technometrics* 60, 4 (2018), 415–429.
- [21] Arnab Hazra, Pratik Nag, Rishikesh Yadav, and Ying Sun. 2024. Exploring the Efficacy of Statistical and Deep Learning Methods for Large Spatial Datasets: A Case Study. *Journal of Agricultural, Biological and Environmental Statistics* (2024), 1–24.
- [22] Matthias Katzfuss and Joseph Guinness. 2021. A general framework for Vecchia approximations of Gaussian processes. *Statist. Sci.* 36, 1 (2021), 124–141.
- [23] Matthias Katzfuss, Joseph Guinness, Wenlong Gong, and Daniel Zilber. 2020. Vecchia approximations of Gaussian-process predictions. *Journal of Agricultural, Biological and Environmental Statistics* 25 (2020), 383–414.
- [24] Matthias Katzfuss, Joseph Guinness, and Earl Lawrence. 2022. Scaled Vecchia approximation for fast computer-model emulation. *SIAM/ASA Journal on Uncertainty Quantification* 10, 2 (2022), 537–554.
- [25] Dmitri Kochkov, Janni Yuval, Ian Langmore, Peter Norgaard, Jamie Smith, Griffin Mooers, Milan Klöwer, James Lottes, Stephan Rasp, Peter Düben, et al. 2024. Neural general circulation models for weather and climate. *Nature* 632, 8027 (2024), 1060–1066.
- [26] Earl Lawrence, Katrin Heitmann, Juliana Kwan, Amol Upadhye, Derek Bingham, Salman Habib, David Higdon, Adrian Pope, Hal Finkel, and Nicholas Frontiere. 2017. The mira-titan universe. II. Matter power spectrum emulation. *The Astrophysical Journal* 847, 1 (2017), 50.
- [27] Crystal Linkletter, Derek Bingham, Nicholas Hengartner, David Higdon, and Kenny Q Ye. 2006. Variable selection for Gaussian process models in computer experiments. *Technometrics* 48, 4 (2006), 478–490.
- [28] Sagnik Mondal, Sameh Abdulah, Hatem Ltaief, Ying Sun, Marc G Genton, and David E Keyes. 2023. Tile low-rank approximations of non-Gaussian space and space-time Tukey g-and-h random field likelihoods and predictions on large-scale systems. *J. Parallel and Distrib. Comput.* 180 (2023), 104715.
- [29] Kevin P Murphy. 2012. *Machine Learning: A Probabilistic Perspective*. MIT Press.
- [30] Qilong Pan, Sameh Abdulah, Marc G Genton, David E Keyes, Hatem Ltaief, and Ying Sun. 2024. GPU-accelerated Vecchia approximations of Gaussian processes for geospatial data using batched matrix computations. In *ISC High Performance 2024 Research Paper Proceedings (39th International Conference)*. Prometheus GmbH, 1–12.
- [31] Qilong Pan, Sameh Abdulah, Marc G Genton, and Ying Sun. 2025. Block Vecchia Approximation for Scalable and Efficient Gaussian Process Computations. *Technometrics* just-accepted (2025), 1–18.
- [32] Carl Edward Rasmussen and Christopher KI Williams. 2006. *Gaussian Processes for Machine Learning*. MIT Press.
- [33] Andrea Saltelli, Paola Annoni, Ivano Azzini, Francesca Campolongo, Marco Ratto, and Stefano Tarantola. 2010. Variance based sensitivity analysis of model output. Design and estimator for the total sensitivity index. *Computer Physics Communications* 181, 2 (2010), 259–270.
- [34] Mary Lai O Salvaña, Sameh Abdulah, Hatem Ltaief, Ying Sun, Marc G Genton, and David E Keyes. 2022. Parallel space-time likelihood optimization for air pollution prediction on large-scale systems. In *Proceedings of the Platform for Advanced Scientific Computing Conference*. 1–11.
- [35] Thomas J Santner, Brian J Williams, William I Notz, and Brain J Williams. 2003. *The design and analysis of computer experiments*. Vol. 1. Springer.
- [36] Jianwei Shi, Sameh Abdulah, Ying Sun, and Marc G Genton. 2025. Decentralized Inference for Distributed Geospatial Data Using Low-Rank Models. *arXiv preprint arXiv:2502.00309* (2025).
- [37] Volker Springel. 2005. The cosmological simulation code GADGET-2. *Monthly Notices of the Royal Astronomical Society* 364, 4 (2005), 1105–1134.
- [38] Alessio Spurio Mancini, Davide Piras, Justin Alsing, Benjamin Joachimi, and Michael P Hobson. 2022. CosmoPower: emulating cosmological power spectra for accelerated Bayesian inference from next-generation surveys. *Monthly Notices of the Royal Astronomical Society* 511, 2 (2022), 1771–1788.
- [39] Furong Sun, Robert B Gramacy, Benjamin Haaland, Earl Lawrence, and Andrew Walker. 2019. Emulating satellite drag from large simulation experiments. *SIAM/ASA Journal on Uncertainty Quantification* 7, 2 (2019), 720–759.
- [40] Aldo V Vecchia. 1988. Estimation and model identification for continuous spatial processes. *Journal of the Royal Statistical Society Series B: Statistical Methodology* 50, 2 (1988), 297–312.
- [41] David J Walters, Ayan Biswas, Earl C Lawrence, Devin C Francom, Darby J Luscher, D Anthony Fredenburg, Kelly R Moran, Christine M Sweeney, Richard L Sandberg, James P Ahrens, et al. 2018. Bayesian calibration of strength parameters using hydrocode simulations of symmetric impact shock experiments of Al-5083. *Journal of Applied Physics* 124, 20 (2018).
- [42] Munir A Winkel, Jonathan W Stallrich, Curtis B Storlie, and Brian J Reich. 2021. Sequential optimization in locally important dimensions. *Technometrics* 63, 2 (2021), 236–248.